

Statistical analysis of subnanometer residual disorder in photonic crystal waveguides: Correlation between slow light properties and structural properties

N. Le Thomas, Z. Diao, H. Zhang, and R. Houdré

*Institut de Physique de la Matière Condensée, École Polytechnique Fédérale de Lausanne (EPFL),
Station 3, CH-1015 Lausanne, Switzerland*

(Received 21 January 2011; accepted 28 June 2011; published 18 August 2011)

The authors present a statistical study of residual disorder in nominally identical planar photonic crystal waveguides operating in the slow light regime. The focus is on the role played by the subnanometer scaled residual disorder inherent to state-of-the-art electron-beam (EB) lithography systems, in particular, on the impact of the nature of the residual disorder on the maximum value of the guided mode group index. The authors analyze the statistical properties of the surface area, the position, and the shape of the air holes that define the photonic crystal with optimized scanning electron microscope micrographs. The authors identify the hole-area fluctuation as the main source of degradation of the dispersive slow light regime by correlating such a microscopic analysis of the structural disorder with large field-of-view optical characterizations based on a Fourier space imaging technique. The structure with the largest group index ($n_g = 40$) exhibits a standard deviation σ of the radius of the hole as low as 0.4 nm. Such a low value of σ , which already significantly limits the maximum achievable group index of the guided mode, stresses the drastic impact of the residual disorder on the performances of the slow light regime. A mean square analysis of the electronic micrographs reveals that the standard deviation of the hole position is lower than an upper limit of 0.6 nm. This upper bound comes from the intrinsic imperfections of the scanning electronic microscope itself, which hinders to quantify the position disorder induced by the EB lithography system. The authors have identified no correlation between the shape of the holes and the group index as for the hole position. As a result, the hole-area fluctuation is currently the main parameter to control in order to improve the performance of the slow light regime. © 2011 American Vacuum Society. [DOI: 10.1116/1.3622289]

I. INTRODUCTION

Planar photonic crystal waveguides are integrated nanostructures that can slow down the speed of light pulses within a photonic chip.^{1,2} Such a property can be used to enhance nonlinear effects or to make delay lines.² The large degree of freedom to engineer the dispersion curve in these structures allows to design structures with ideally vanishing group velocity. The dispersion curve is defined by the relation $\omega(k)$, where ω is the angular frequency and k is the wave number of the wave.

In practice; however, the minimal group velocity v_g is limited by any residual imperfections resulting from the technological fabrication, although the maturity of the electron beam (EB) lithography technique gives access to subnanometer scale resolution. Even with state-of-the-art tools, typical sizes of imperfections that come into play scale down to the subnanometer range.³ At such a scale, the identification and quantification of the nature of the residual disorder becomes challenging. Even though the local information of the 1 nm root mean square roughness can be inferred from transmission electron microscope micrograph,⁴ a more complete determination of the disorder requires the knowledge of correlation functions, whose correlation length can be as large as 10 μm . The main issue in identifying large-scale correlation lengths for disorder fluctuation ranging in the subnanometer scale comes from the

requirement of both large field-of-view and high-resolution microscopy tools.

The current residual imperfections scale with the resolution of large field-of-view characterization tools, as can be seen in the case of the most recent conventional scanning electron microscopes (SEM) (around 1.5 nm for an acceleration voltage of 6 keV). The distinction between a characterization of the measuring apparatus, i.e., the SEM, and a characterization of the sample itself is particularly difficult for the lowest residual disorder that can be currently achieved. This issue is well pointed out in Ref. 5 where it is clearly emphasized, “reconstruction of actual dielectric profiles from SEM images can be a very nontrivial task far beyond the scope of this paper. In the following we apply our statistical analysis to SEM images assuming that they represent true dielectric profiles.”

One of the objectives of the current paper is to show that optimized scanning electron microscope micrographs can actually identify the nature of the subnanometer residual disorder inherent to present state-of-the-art EB lithography. We base our analysis on a systematic comparison with the optical properties of an ensemble of nominally identical W1 photonic crystal waveguides. Such an analysis allows us to identify the imperfection resulting from the characterization tools themselves and to highlight correlations between the properties of the residual disorder and the ones of the light propagation.

The optical properties of the slow light regime are particularly sensitive to the residual disorder and can be conveniently measured with large field-of-view optical microscopes. We have recently highlighted that different light transport regimes can take place depending on the amount of structural imperfections and on the dispersive properties of the underlying ideal structure.⁶ We have used a Fourier space imaging technique that provides a direct image of the dispersion curve and allows us to determine accurately the group velocity in photonic crystal waveguides. Moreover, this optical technique can determine specific loss channels that are activated by the nature of the autocorrelation function of the residual disorder in the photonic structures. For instance, residual periodic corrugation inherent to the fabrication process of EB patterning and not detectable with conventional SEM can be optically tracked as demonstrated in Ref. 7 where the correlation length of $1.28 \mu\text{m}$ inferred from the Fourier space imaging technique was found to match exactly the trapezoidal write subfield pattern used during the EB lithography process.

Each individual photonic structure corresponds to a single realization of disorder. Even though it can provide useful information about the origin of some optical loss channels, a statistical study over several realizations is, in general, required to characterize a disorder distribution, as well as its impact on the optical properties of a particular photonic design. In particular, recent theoretical predictions of the impact of residual disorder on the slow light regime are based on an averaging of different configurations of the disordered dielectric map for a given structure with the assumption of Gaussian distributions.^{8–10} Although such theoretical approaches constitute guidelines for the understanding of the impact of residual disorder, they always start with an *a priori* choice of the statistical distribution of the disorder. There is currently no direct link between theoretical modeling and disorder distribution in *real* structures. The optical properties of a typical design have been experimentally investigated for only one single realization, except for a recent report,¹¹ which does not permit to infer the statistical nature of the disorder, and to identify the major obstacles of a fabrication process. There is also no systematic study on the statistical nature of the disorder in Ref. 11. Here, we will show that the distributions can be more complex than Gaussian distributions.

In this paper we perform a statistical analysis of the residual disorder on an ensemble of 20 W1 photonic waveguides that have been fabricated with state-of-the-art EB lithography. We focus on the correlations between the different aspects of the structural disorder and the optical properties of the nominally identical waveguides. The photonic crystal pattern is analyzed with optimized SEM images, whereas the optical properties are inferred from the direct measurement of the dispersion curves in the Fourier space. Issues related to resolution and SEM imperfection are highlighted. The simultaneous advanced analysis of the dispersion curves and of the SEM image allows us to identify the imperfections intrinsic to the sample fabrication. As a result, we highlight the current nature of the structural disorder that limits the

performances of the slow light regime in planar PhC waveguides.

II. DESIGN AND FABRICATION

As recently reported, the optical dispersive properties of W1 photonic crystal waveguides fabricated in high contrast semiconductor material are very sensitive to any residual disorder.⁶ The impact of the residual disorder near a photonic band edge is highlighted by a well-defined transition in the dispersion curve between a dispersive regime and a diffusive regime. In the dispersive regime that corresponds to a well-defined dispersion curve $\omega(k)$, a group index n_g or equivalently a group velocity v_g can be defined.¹⁰ No function $\omega(k)$ can be defined anymore in the diffusive regime. The group index at the transition reaches a maximum value that depends on the amount of residual disorder with a high precision, as will be presented in the following. It follows that the maximum achievable n_g in a W1 waveguide constitutes a convenient indicator of the impact of the disorder.

PhC cavities can also be used to study the structural imperfections.^{12,13} However; in contrast to cavities, a W1 PhC waveguide that is defined by one single line of missing holes along the ΓK direction in a two-dimensional triangular photonic lattice (see Fig. 1) is invariant per translation. It follows that such a design is well suited to infer the long-range statistical nature of the disorder and its resulting impact on the Bloch modes over a large field. Note that with 2D pattern

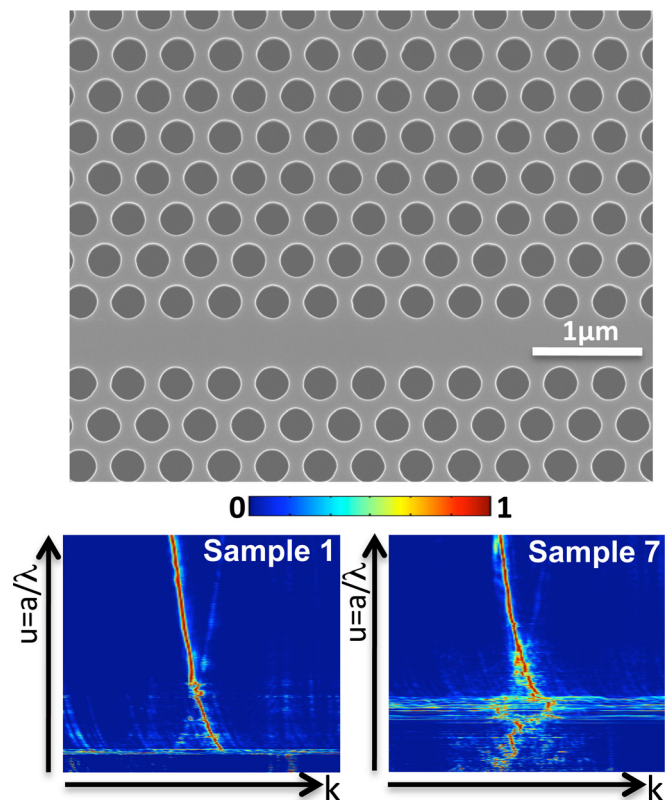


Fig. 1. (Color online) (Top) Optimized scanning electron micrograph of the W1 photonic crystal waveguide corresponding to sample 1 (2560×2048 pixels; 1 pixel = 2.085 nm). (Bottom) Experimental dispersion map for sample 1 (left) and sample 7 (right).

the Bloch modes are delocalized over a larger area; however, near a 2D band edge the transition between the dispersive and the diffusive regime does not exhibit the sharp transition observed in the 1D case, which provides a less sensitive platform to investigate the nature of residual disorder.¹⁴ It has to be stressed that the photonic band edge that we investigate here in the W1 waveguide is located below the light cone. The broadening of the spatial frequencies spectrum inherent to the disorder overcomes in consequence the smooth broadening induced by decoherence effect intrinsic to out-of-plane losses, i.e., pure dissipation.¹⁵

We have fabricated 20 nominally identical W1 waveguides on the same silicon-on-insulator (SOI) chip. The top Si layer and the buried oxide layer were 220 nm and 2 μm thick, respectively. The waveguides were designed for operating in a wavelength range of 1.5 μm , with a lattice constant $a = 440$ nm. The photonic crystal was patterned with a Vistec EBPG5000 electron beam lithography system operating at 100 keV beam energy. The beam step size resolutions, the number of vertices used to define the holes, the writing field, and the maximum trapezium subfields were 2.5 nm, 68, 160 $\mu\text{m} \times 160$ μm , and 4.525 μm , respectively. ZEP-520A positive-tone EB resist was used as the etching hard mask. The transfer of the pattern from the ZEP to the Si core layer was performed in a single step, using inductively coupled plasma etching with a combination of SF_6 and C_4F_8 gas. The buried oxide layer was removed by etching for 30 min in fluoric-based acidic solution to release a freestanding silicon membrane.

III. OPTICAL MEASUREMENT

We have measured the dispersion curves with a high numerical aperture Fourier space image technique described in Ref. 16 in order to determine the largest group index n_g^{max} that can be achieved for each PhC waveguide. The value of the wave number k is directly determined with such a technique in the back focal plane of the collecting microscope objective for each excitation frequency ω . We have integrated probe gratings on both sides of the external boundaries of the bulk PhC pattern as explained in Ref. 17 as the photonic band edge is located below the light cone in the current study. These gratings whose elementary cell consists of two extra holes similar to the holes of the bulk PhC pattern allows us to fold the dispersion curve into the light cone and to detect the signal in the optical far field with a controlled minimal disturbance. In Fig. 1, we show two typical dispersion maps of nominally identical W1 waveguides, labeled as sample 1 and sample 7. In each case, a well-defined dispersion curve, that corresponds to the so-called dispersive regime evolves toward a speckle-like pattern when the reduced frequency $u = a/\lambda = a\omega/(2\pi c)$ decreases toward the mode band edge. This speckle-like pattern is the signature of a diffusive regime,¹⁵ where the group velocity losses relevance. The sample 1 has a maximum group index of $n_g^{\text{max}} = 40$, which is the largest value determined among the set of all the waveguides.

The search for a reliable correlation between the optical and the structural properties of the waveguides requires the determination of the experimental group index with a high

accuracy. Each experimental dispersion curve was fit with a guided mode expansion theoretical model¹⁸ to achieve such a high accuracy, as shown in Fig. 2 for samples 1 and 5. The experimental dispersion curves were obtained from the position of the peak maximum of the far-field spectrum. The fit procedure allows us to accurately identify the frequency ω_t at the transition between the dispersive and the diffusive regime, which is highlighted by a horizontal dash line for each sample in Fig. 2. The theoretical group index dispersion curve $n_g(u)$ (red/gray cross-dot curve) can be simply deduced from the theoretical dispersion curve $\omega(k)$ (blue/dark square-dot curve). The group index maximum n_g^{max} is determined from the intersection between the horizontal dashed line at ω_t and the $n_g(u)$ curve and identified with a vertical dashed line. The value of ω_t is cross-checked with the onset of an abrupt enhanced scattering intensity in the out-of-plane spectrum.

This fitting procedure of the dispersion curve provides in addition the filling factor f that is proportional to the mean area of the holes A_m and that is defined by $f = (2\pi/\sqrt{3})(r/a)^2$ for each PhC waveguide. Concomitantly, A_m was determined from the SEM images for each waveguide, as will be explained in the following. The filling factor and the mean area of the holes follow the same variation according to the sample number as shown in Fig. 3. We also observe a variation of the size of the holes although the waveguides were nominally identical. The part of the SOI wafer used to

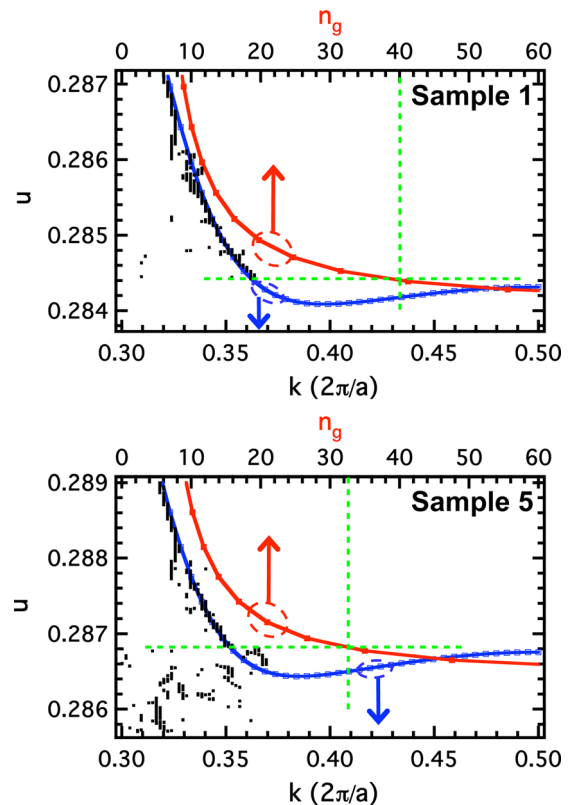


FIG. 2. (Color online) Experimental (dark points) and theoretical (blue dot line) dispersion curves for sample 1 (top) and sample 5 (bottom), as well as theoretical group index dispersion curve (red dot line). The dashed green lines highlight the position of the maximum experimental group index for each sample.

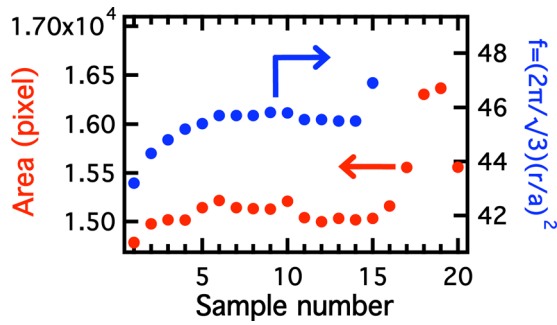


FIG. 3. (Color online) Variations of the hole area (red circles) and of the filling factor f (blue circles) vs the sample number. The holes area and the filling factor f are determined from SEM images and from the experimental dispersion curve, respectively.

pattern the PhC structures was selected in a region where the thickness of the Si and buried oxide layers shows no apparent variations as controlled with ellipsometry measurement over the entire wafer. Besides, along the 160 μm long waveguides, no significant variation of the mean size of the holes was detected. We definitively exclude the fluctuation of the SOI layers thickness given that the waveguides are separated by 50 μm . We can identify two possible effects that cause the filling factor variations: First some variations of the thickness of the EB resist inherent to the spinning procedure, second some variations of the current during the EB lithography from sample to sample.

The light does not propagate through the waveguide when the sizes of the holes correspond to a filling factor larger than 48%, and as a result the filling factor cannot be extracted from the measurement of the dispersion curve. We attribute the loss of waveguide transmission to an enhanced impact of the residual disorder, which is confirmed by the fact that the observed larger filling factor is correlated with a larger standard deviation of the size of the holes.

IV. SEM ANALYSIS

The spatial resolution of the SEM microscope used to analyze the structural patterns of the different W1 waveguides was ~ 2 nm (acceleration voltage 10 kV, working distance 6.3 mm). We have matched the pixel size to this resolution by selecting a sample area of $5.34 \mu\text{m} \times 4.27 \mu\text{m}$ with a large pixel density (2560×2048 pixels and 1 pixel corresponds to 2.085 nm) as shown in Fig. 1(a). The selected sample area provides a number of holes as large as 99 that is sufficient for a statistical analysis. The SEM micrograph is taken at the same place of the waveguide for each structure in order to guarantee identical conditions for the statistical analysis. We have used the threshold method of Otsu,¹⁹ which converts the SEM grayscale intensity image to a binary image to analyze the size, the position, and the shape of the hole. One particular map generated by this procedure is shown in Fig. 4. As a result, the total number of dark pixels that define a hole directly provides the effective surface area of the hole. The determination of an accurate absolute value of the size is difficult due to the electron

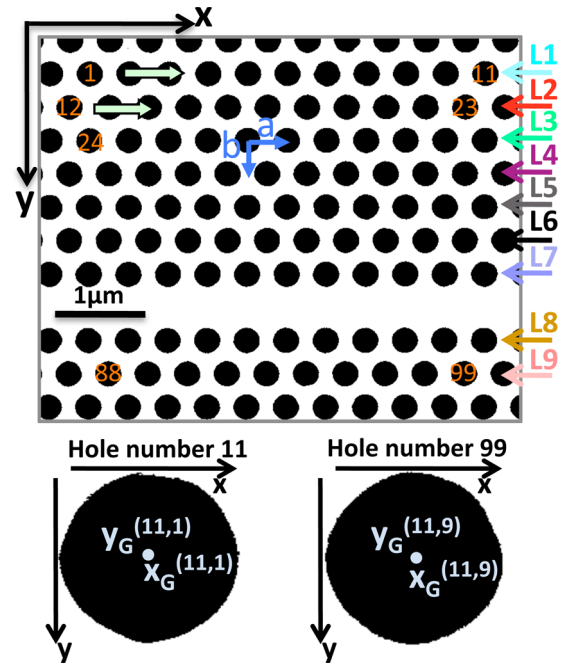


FIG. 4. (Color online) Binary image obtained from the SEM micrograph as the one presented in Fig. 1. (Bottom) Zoom of hole numbers 11 and 99.

scattering at the hole edges, which is intrinsic to scanning electron microscopy. Nevertheless, such an absolute value is not required here as we are mainly concerned with the statistical properties of the geometrical parameters from holes to holes. The coordinates (x_G^{ij}, y_G^{ij}) of the barycenter of the dark pixels define the position of the hole (i, j) . All the holes are numbered along the direction of the lines as indicated in Fig. 4, which allows us to create sets of holes per line from line L1 to line L9.

A. Hole size fluctuation

The typical number of pixels that form a single hole is $\sim N_p \approx 1.5 \times 10^4$ as highlighted in Fig. 3. If we assume that the different sources of noise obey Poisson statistics, the fluctuation of the number of pixels between different holes is $\sqrt{N_p} \approx 160$. Averaging over 99 holes allows us to reach an uncertainty of around 2 pixels on the mean area of the hole. The variation of the area of the holes for two typical waveguides, samples 4 and 6 are reported in Fig. 5. For sample 6, the histogram of the area values corresponds to a Poisson distribution with the variance roughly equal to the mean pixel number of the area. The envelope of the histogram seems to tend toward a normal distribution as expected for large mean area values and for a residual disorder of Gaussian type. In the case of sample 4, the histogram is more complex and cannot be associated with a Poisson distribution. If the variation of the area of the holes is plotted for each hole and grouped per line, as at the bottom of Fig. 5, two different distributions are visible: one is intrinsic to all the holes and the other is peculiar to a given line. The last distribution is highlighted by large jumps of the mean area per line from line to line in an erratic way. These jumps can

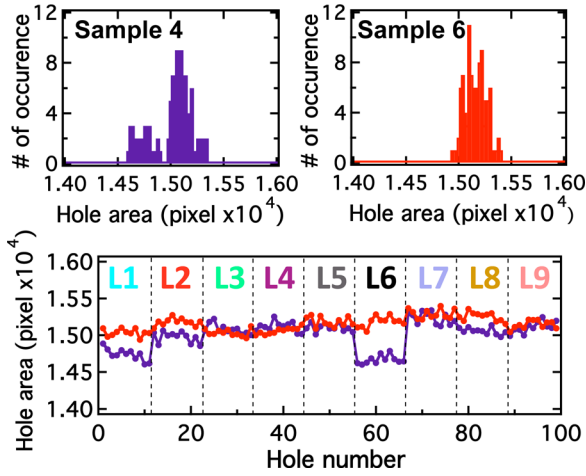


Fig. 5. (Color online) (Top) Hole area distribution for sample 4 (left) and sample 6 (right) obtained from images similar to the one shown in Fig. 4. (Bottom) Variation of the hole area vs the holes number as labeled in Fig. 4

be attributed to some variations of the electron beam current either during the SEM scan or during the EB lithography. During the EB patterning, the lines of holes are exposed one after the other, which can induce random beam current fluctuation from line to line. For some of the samples the pattern was measured at the beginning and at the end of the 160- μm -long W1 waveguides with no significant modification of the statistic per line. The length of the waveguide was chosen to match the writing field in order to avoid any issues related to stitching errors. Moreover, the length matches the current field of view of the optical Fourier space setup, which can be increased by lowering the numerical aperture of the collecting microscope objective.

The fluctuation of the mean area of the holes from line to line is not expected to decrease the performance of the waveguides. Such kind of variation does not break the invariance per translation and modify globally the dispersion curve of the waveguide. Nevertheless, different designs can be more

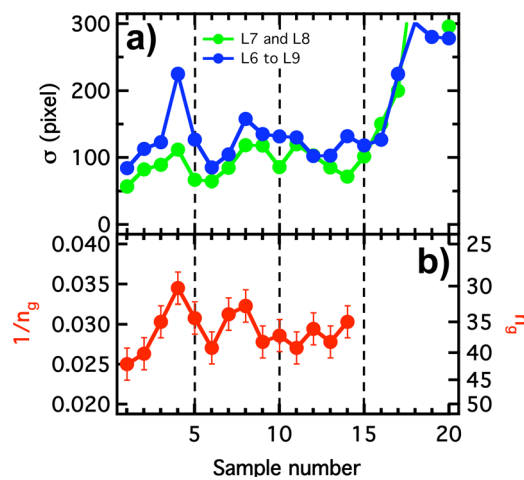


Fig. 6. (Color online) (Top) Variation of the holes size standard deviation for lines L7 and L8 (green dots) and for lines L6–L9 (blue dots), vs the sample number. (Bottom) Variation of the group index n_g vs the sample number.

or less sensitive to the disorder and the disorder-induced coupling between different modes, such as the odd and even modes, can be enhanced.²⁰

In Fig. 6, the standard deviation of the hole area σ is plotted for each sample and compared with the variations of the maximum group index n_g and of the normalized group velocity $v_g/c = 1/n_g$. In order to minimize the impact of the fluctuations related to the jump of the mean area value per line, the standard deviation σ has been calculated for a set of holes that corresponds to the first 2 lines, L7 and L8 on each sides of the waveguide core, as well as for another set formed by the four lines, L6–L9. These first and second sets of holes are associated with a pixel noise of 8 and 4 pixels, respectively. The variation of σ from sample to sample is roughly identical between these two sets. In terms of impact on the optical properties, these two sets are the most relevant as the field of the mode is mainly concentrated in the core. A weighting factor for lines L6 and L9 in the averaging of σ over the four lines could be added for a finer analysis to take into account the modification of the transverse profile of the guided mode from line to line.

Figure 6 reveals a good correlation of the variation of σ and $1/n_g$ within the error bar associated with $1/n_g$. These error bars come from the uncertainty that is linked with the fitting procedure of the experimental dispersion curve. If a mean effective radius R_{eff} is associated with a perfect circular hole of the same area as the measured mean value, the minimum fluctuation of the size of the hole is as low as 0.3% for a maximum n_g of 40. This corresponds to a standard deviation of R_{eff} of 0.4 nm. The observed correlation between the variation of σ and $1/n_g$ implies that the determination of the nature of the statistical distribution over a waveguide length of 5.3 μm is, in the first approximation, sufficient to infer the properties of the whole structure, provided that for a particular structure the disorder is homogeneous over all the waveguide.

B. Hole position fluctuation

In order to determine the statistical nature of the fluctuations of the positions (x_G^{ij}, y_G^{ij}) of the holes from the ideal triangular lattice we used a least square fit method. This method is more convenient than the 2D Fourier analysis of the SEM micrograph.²¹ It consists of finding the parameters of the actual triangular lattice, i.e., the two lattice vectors $\vec{a} = a_x \vec{x} + a_y \vec{y}$, $\vec{b} = b_x \vec{x} + b_y \vec{y}$, and the origin (x_0, y_0) that minimizes the sum of the square of distance r_{ij} between the ideal position and the measured one:

$$\sum_{ij} r_{ij}^2 = \sum_{ij} \left\{ \left[(x_0 + ia_x + jb_x) - x_G^{ij} \right]^2 - \left[(y_0 + ia_y + jb_y) - y_G^{ij} \right]^2 \right\}. \quad (1)$$

As an example, a_x and b_x are solutions of the following system:

$$\left\{ \begin{aligned} \left[\sum_{i,j} i^2 - \frac{\left(\sum_{i,j} i\right)^2}{\sum_{i,j} 1} \right] a_x + \left[\sum_{i,j} ij - \frac{\sum_{i,j} i \sum_{i,j} j}{\sum_{i,j} 1} \right] b_x &= \sum_{i,j} \left(i x_G^{i,j} \right) - \frac{\sum_{i,j} i}{\sum_{i,j} 1} \sum_{i,j} x_G^{i,j} \\ \left[\sum_{i,j} ij - \frac{\sum_{i,j} i \sum_{i,j} j}{\sum_{i,j} 1} \right] a_x + \left[\sum_{i,j} j^2 - \frac{\left(\sum_{i,j} j\right)^2}{\sum_{i,j} 1} \right] b_x &= \sum_{i,j} \left(j x_G^{i,j} \right) - \frac{\sum_{i,j} j}{\sum_{i,j} 1} \sum_{i,j} x_G^{i,j}, \end{aligned} \right. \quad (2)$$

where i and j indices are the hole numbers between 1 and 99. It is important to stress that the nominal parameters of the lattice are not incorporated into the least square fit; the only input parameters are the barycenter coordinates of the holes. Any deviation from the nominal ideal lattice, such as a shear deformation, is retrieved from the least square fit. In addition, any tilt of the SEM image with regards to the x and y axes are taken into account and compensated by the degree of freedom in the angular orientation of the two lattice vectors. The fluctuations of the position of the different holes (i,j) are directly given with the vectors \vec{r}_{ij} when the ideal lattice parameters are determined. The resulting ensemble of all the vectors $\vec{r}_{ij} = \Delta X_G \vec{x} + \Delta Y_G \vec{y}$ of the SEM images of the 20 W1 waveguides is plotted in Fig. 7. The distribution of this ensemble tends toward an isotropic Gaussian distribution. As shown by the histograms in the ΔX_G and ΔY_G directions, the standard deviation is ~ 1.3 nm similar to the one recently reported.¹³ A deeper analysis of the distribution of the position of the holes for each sample reveals, however, a more complex underlying statistics, as highlighted by the Figs. 8(a)–8(c). These figures show that the fluctuations of

the position of the holes are strongly correlated per line, with a cloud of holes well defined for each line. In addition, each cloud shifts in different directions and with different magnitudes depending on the sample, which ends up in a Gaussian distribution after averaging the position fluctuation over all samples. The fracturation procedure of the source file that codes the PhC pattern (each hole is broken down into 33 trapezoids) is the same for all the 20 waveguides. We can therefore conclude that the fracturation process is not responsible for the observed position fluctuation of the line as a given line of holes exhibits a different spatial shift according to the sample number.

In Fig. 8, the positions of the holes are deduced from a SEM micrograph, where the lines of the PhC pattern are aligned with the fast horizontal scan axis of the SEM. We have rotated the sample by 90° from the fast horizontal scan axis, i.e., line number 1 for instance is along the y axis instead of the x axis (see Fig. 4 for the axis orientation) in order to search any correlation between the position of the holes and the scanning procedure. As a result, the previously observed correlation per PhC line for the fluctuations of the position of

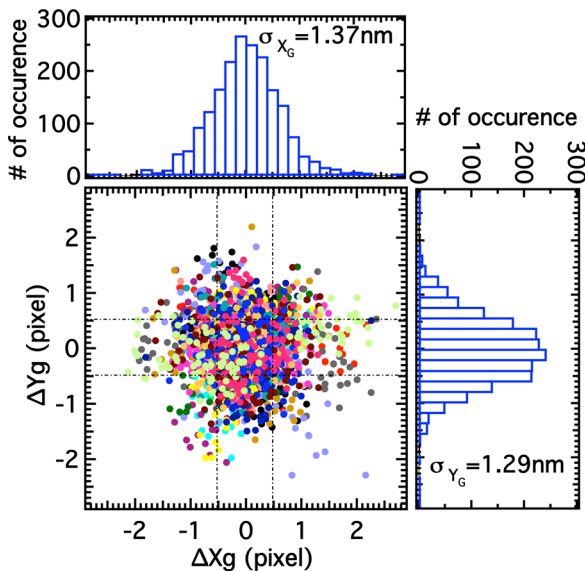


FIG. 7. (Color online) Deviation of the hole barycenters from the ideal photonic crystal lattice. Each color (99 dots) corresponds to one particular sample for the online version. The dotted–dashed lines highlight the SEM resolution of 1 pixel. At the top and on the right: Distributions of the position fluctuations along the x and y axes, respectively.

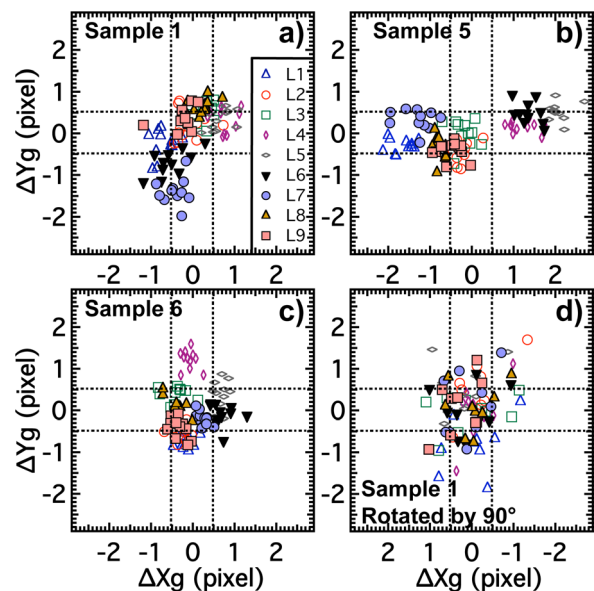


FIG. 8. (Color online) Same as Fig. 7 but for (a) sample 1, (b) sample 5, and (c) sample 6 separately. (d) Same as (a) but with the sample rotated by 90° according to the scanning direction. One color or symbol shape corresponds to one line of PhC holes as labeled in Fig. 4.

the holes disappears: as shown in Fig. 8(d), the clouds of points associated with each line are not distinguishable anymore. Figure 8 clearly shows that the SEM scanning procedure is responsible of the observed correlation of the hole position per line. We attribute the discrete and random variations of the clouds position from line to line to charging effect.

The comparison between the variations of the standard deviation of the shift of the holes $\sigma_{\text{hole shift}}$ and of $1/n_g$ according to the sample clearly reveals no correlations [see Fig. 9(a)] as expected from the previous discussion. The minimum $\sigma_{\text{hole shift}}$ that corresponds to sample 7 is as low as 0.5 nm. Nevertheless this sample is not associated with the largest maximum group index.

We have performed a finer analysis of the disorder relative to the positions of the holes to eliminate the SEM artifacts. It consists in removing the bias related to the shifts of the lines, which is induced by the SEM. The standard deviation for ΔX_G and ΔY_G is calculated per line and then averaged over all the lines to obtain the unbiased standard deviation:

$$\sigma_{\text{hole shift}}^{\text{unbiased}} = \frac{1}{N_L} \sum_{i=1}^{N_L} \sigma_{\text{hole shift}}^{L_i}$$

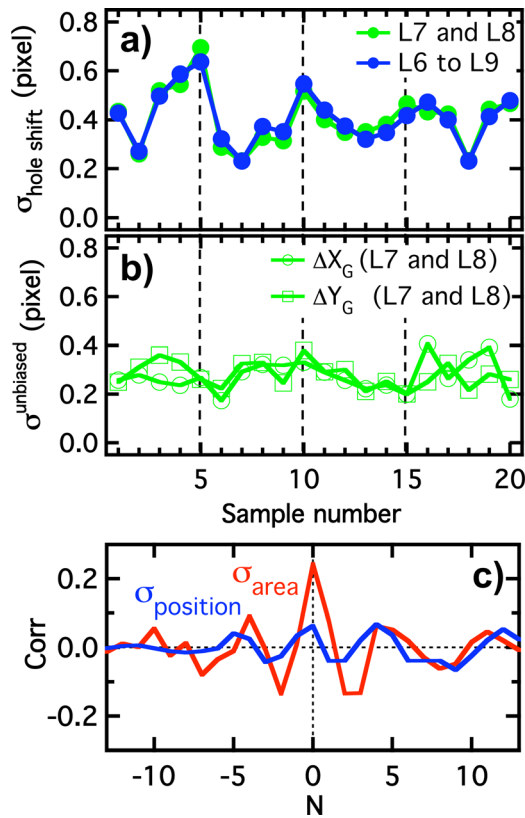


FIG. 9. (Color online) (a) Standard deviation of the holes position for lines L7 and L8 (green dots) and for lines L6–L9 (blue dots), vs the sample number. (b) Same as the top but with the correction of the bias induced by the SEM microscope. (c) Red line: Correlation function between the variation of the inverse of the group index $1/n_g$ [Fig. 6(b)] vs the sample number and the variation of the holes area standard deviation vs the sample number [Fig. 6(a)]. Blue line: Correlation function between the variation of $1/n_g$ vs the sample number and the variation of the holes area standard deviation vs the sample number (b).

where N_L is the total number of lines. The unbiased standard deviation is almost constant for the 20 samples compared to the fluctuations of $\sigma_{\text{hole shift}}$ from sample to sample, reported in Fig. 9(a). The mean standard deviation is 0.6 nm in both the X and Y directions. The comparison between the variations of $\sigma_{\text{hole shift}}^{\text{unbiased}}$ according to the sample number in Fig. 9(b) with the ones of $1/n_g$ in Fig. 6(b) does not seem to reveal any correlation. In Fig. 9(c) the correlation function (blue/dark curve) between the variation of the position of the holes versus the sample number [Fig. 9(a)] and the variation of $1/n_g$ [Fig. 6(b)] confirms the absence of any impact of the position disorder on the slow light regime for the current state-of-the-art EB lithography. In contrast, the correlation function (red/light curve) between the variation of the area of the holes versus the sample number [Fig. 6(a)] and the variation of $1/n_g$ [Fig. 6(b)] exhibits a significant peak at the origin that is twice as large as the background noise. This peak is a clear signature of the correlation between the fluctuation of the hole area and the maximum group index.

C. Holes shape fluctuation

The profile of each hole can be represented from the binary image (see Fig. 4) in a polar plot with the origin defined by (x_G^{ij}, y_G^{ij}) , as shown in Figs. 10 and 11 for samples 1 and 4, respectively. We have superimposed the profiles of the 11

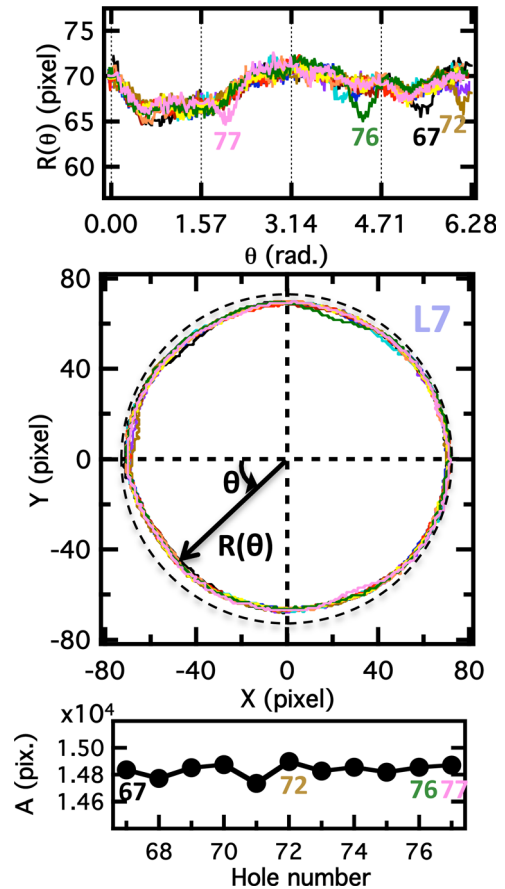


FIG. 10. (Color online) Shape profiles of the holes for the line 7 of sample 1. (Top) Polar plot, (Middle) Cartesian plot, (Bottom) Variation of the holes area in pixel vs the holes number.

holes that belong to a given line (line L7 in Figs. 10 and 11). Such superimposed profiles present no difference in the global shape apart from rare localized defects along the different profiles. A slight translational shift of the profile, that we attribute to a tiny rotation of the entire SEM image is revealed by the standard $R(\theta)$ plot. The shape of the hole is not perfectly circular as highlighted by the dashed circle in the polar plot. The deviation from the circular shape is almost the same for both samples. At this stage the departure from the ideal circular shape can equally be explained by the SEM astigmatism or by the sample fabrication.

We have identified, in the A versus hole number plot at the bottom of Fig. 11, the holes that exhibit the previously mentioned localized defects, for instance hole numbers 67, 72, 76, and 77 in the case of sample 1. Such identification aims at verifying if such defects localized along the circumference can explain the fluctuations of the hole area A . The variation of A , according to the hole number shows that a localized defect corresponding to a decrease in $R(\theta)$ does not necessarily imply a decrease in A . The fluctuation of the hole area is a global effect except for very large defects, such as the one observed for hole number 69.

Our experimental data are currently not in a position to reveal any correlation between any variation of the shape of the holes among the PhC pattern and the optical properties of the corresponding structures. It was reported in Ref. 22 that the impact of the surface roughness affects the band edge

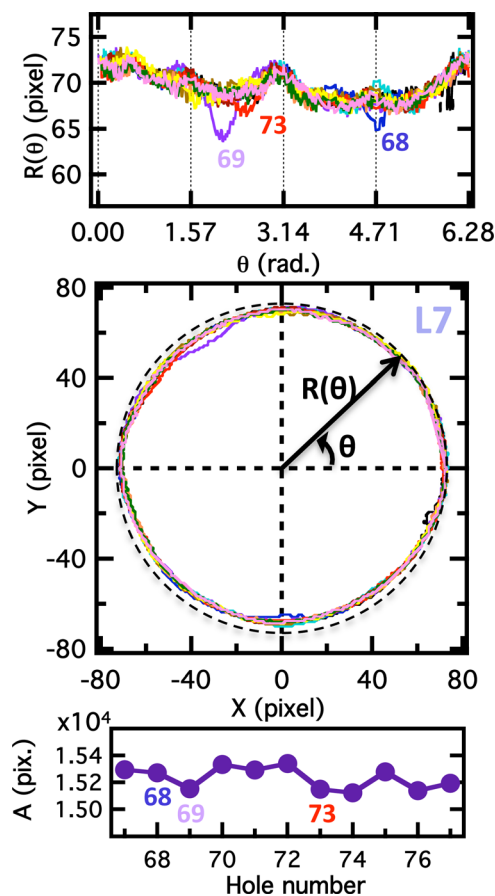


FIG. 11. (Color online) Same as Fig. 10 but for sample 4.

performances of coupled cavity waveguides based on a theoretical model. Our experimental data show that the surface roughness affects the optical performance in the slow light regime more by an induced modification of the area of the holes than by a pure shape disorder. Modeling holes with irregular shapes and using Bloch mode expansion²⁰ also lead to the same observation.²³ Finally, Fig. 9(c) and the hole shape analysis reveal that the disorder associated with the fluctuation of the size of the holes is the main source of limitation of the group index with current state-of-the-art EB lithography.

V. SUMMARY AND CONCLUSIONS

The identification of the properties of the residual disorder in nanophotonic structures requires characterization tools that combine high resolution, high sensitivity to disorder and a large field of view. Far-field optical techniques such as the Fourier space imaging technique provide the high sensitivity in the slow light regime and the large field of view. Scanning electron microscopes can reach nanometer-scale resolution but with limited field of view. We have reported that a careful analysis can give an accurate view of the disorder by combining both the SEM and the Fourier space imaging technique. In particular, the optimized $5\ \mu\text{m} \times 4\ \mu\text{m}$ field of view of SEM microscope allows deducing global information about the current residual disorder, such as correlations per lines of the PhC pattern. Our analysis shows that the fluctuation of the size of the holes is the current major source of degradation of a photonic band edge for state-of-the-art EB lithography. A standard deviation of the size of the hole as low as 0.4 nm limits the group index of W1 waveguides to 40. A mean fluctuation of the position of the holes smaller than 0.6 nm can be inferred from a statistical mean square analysis of the 2 nm resolution SEM images, if correlation effects due to the SEM scan are removed. Finally, we have also investigated the impact of the beam step size (1.25, 2.5, and 5 nm) on other structures. Although a slight broadening of the autocorrelation function of the angular spectra was observed for the beam step size of 5 nm, for a beam step size of 1.25 or 2.5 nm, no impact was clearly seen on the statistical analysis of the SEM images, as well as on the optical properties. It suggests that the EB resolution is not the current main limiting factor to achieve high quality nanophotonic structures.

ACKNOWLEDGMENTS

This work was supported by the Swiss NCCR-Quantum Photonics, the Swiss National Science Foundation (SNSF) (Project No. 200021-124413), and the COST action MP0702. The authors thank P. Ulagalandha Dharanipathy for careful reading of the manuscript and P. Baras for pointing out the least square fit method.

¹T. Baba, *Nature Photon.* **2**, 465 (2008).

²T. F. Krauss, *J. Phys. D Appl. Phys.* **40**, 2666 (2007).

³Y. A. Vlasov, M. O'Boyle, H. F. Hamann, and S. J. McNab, *Nature (London)* **438**, 65 (2005).

⁴J. Takahashi, T. Tsuchizawa, T. Watanabe, and S. Itabashi, *J. Vac. Sci. Technol. B* **22**, 2522 (2004).

- ⁵M. Skorobogatiy, G. Bégin, and A. Talneau, *Opt. Express* **13**, 2487 (2005).
- ⁶N. Le Thomas, H. Zhang, J. Jágerská, V. Zabelin, R. Houdré, I. Sagnes, and A. Talneau, *Phys. Rev. B* **80**, 125332 (2009).
- ⁷J. Jágerská, N. Le Thomas, R. Houdré, J. Bolten, C. Moormann, T. Wahlbrink, J. Čtyroký, M. Waldow, and M. Först, *Opt. Lett.* **32**, 2723 (2007).
- ⁸M. Patterson, S. Hughes, S. Combrié, N.-V.-Quynh Tran, A. De Rossi, R. Gabet, and Y. Jaouën, *Phys. Rev. Lett.* **102**, 253903 (2009).
- ⁹S. Mazoyer, J. P. Hugonin, and P. Lalanne, *Phys. Rev. Lett.* **103**, 063903 (2009).
- ¹⁰N. Le Thomas and R. Houdré, *J. Opt. Soc. Am. B* **27**, 2095 (2010).
- ¹¹S. Mazoyer, P. Lalanne, J. C. Rodier, J. P. Hugonin, M. Spasenovic, L. Kuipers, D. M. Beggs, and T. F. Krauss, *Opt. Express* **18**, 14654 (2010).
- ¹²H. Hagino, Y. Takahashi, Y. Tanaka, T. Asano, and S. Noda, *Phys. Rev. B* **79**, 085112 (2009).
- ¹³W. Fan, Z. Hao, Z. Li, Y. Zhao, and Y. Luo, *J. Lightwave Technol.* **28**, 1455 (2010).
- ¹⁴N. Le Thomas, R. Houdré, D. M. Beggs, and T. F. Krauss, *Phys. Rev. B* **79**, 033305 (2009).
- ¹⁵N. Le Thomas, V. Zabelin, R. Houdré, M. V. Kotlyar, and T. F. Krauss, *Phys. Rev. B* **78**, 125301 (2008).
- ¹⁶N. Le Thomas, R. Houdré, M. V. Kotlyar, D. O'Brien, and T. F. Krauss, *J. Opt. Soc. Am. B* **24**, 2964 (2007).
- ¹⁷N. Le Thomas, R. Houdré, L. H. Frandsen, J. Fage-Pedersen, A. V. Lavrinenko, and P. I. Borel, *Phys. Rev. B* **76**, 035103 (2007).
- ¹⁸L. C. Andreani and D. Gerace, *Phys. Rev. B* **73**, 235114 (2006).
- ¹⁹N. Otsu, *IEEE T. Syst. Man Cyb. SMC-9*, 62 (1979).
- ²⁰V. Savona, *Phys. Rev. B* **83**, 085301 (2011).
- ²¹R. Ferrini, D. Leuenberger, R. Houdré, H. Benisty, M. Kamp, and A. Forchel, *Opt. Lett.* **31**, 1426 (2006).
- ²²D. P. Fussell, S. Hughes, and M. M. Dignam, *Phys. Rev. B* **78**, 144201 (2008).
- ²³V. Savona, private communication, December 31, 2010.